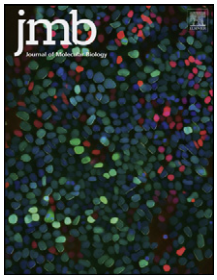

The SARS-CoV Fusion Peptide Forms an Extended Bipartite Fusion Platform that Perturbs Membrane Order in a Calcium-Dependent Manner

Alex L. Lai [1], Jean K. Millet [2], Susan Daniel [3], Jack H. Freed [1] and Gary R. Whittaker [2]

*1 - **Department of Chemistry and Chemical Biology,** Cornell University, Ithaca, NY 14853, United States*
*2 - **Department of Microbiology and Immunology,** Cornell University, Ithaca, NY 14853, United States*
*3 - **School of Chemical and Biomolecular Engineering,** Cornell University, Ithaca, NY 14853, United States*

***Correspondence to Jack H. Freed and Gary R. Whittaker:** gary.whittaker@cornell.edu, jhf3@cornell.edu*
https://doi.org/10.1016/j.jmb.2017.10.017
Edited by P-Y Lozach

Abstract

Coronaviruses (CoVs) are a major infectious disease threat and include the pathogenic human pathogens of zoonotic origin: severe acute respiratory syndrome CoV (SARS-CoV) and Middle East respiratory syndrome CoV (MERS-CoV). Entry of CoVs into host cells is mediated by the viral spike (S) protein, which is structurally categorized as a class I viral fusion protein, within the same group as influenza virus and HIV. However, S proteins have two distinct cleavage sites that can be activated by a much wider range of proteases. The exact location of the CoV fusion peptide (FP) has been disputed. However, most evidence suggests that the domain immediately downstream of the S2′ cleavage site is the FP (amino acids 798–818 SFIEDLLFNKVTLADAGFMKQY for SARS-CoV, FP1). In our previous electron spin resonance spectroscopic studies, the membrane-ordering effect of influenza virus, HIV, and Dengue virus FPs has been consistently observed. In this study, we used this effect as a criterion to identify and characterize the *bona fide* SARS-CoV FP. Our results indicate that both FP1 and the region immediately downstream (amino acids 816–835 KQYGECLGDINARDLICAQKF, FP2) induce significant membrane ordering. Furthermore, their effects are calcium dependent, which is consistent with *in vivo* data showing that calcium is required for SARS-CoV S-mediated fusion. Isothermal titration calorimetry showed a direct interaction between calcium cations and both FPs. This Ca^{2+}-dependency membrane ordering was not observed with influenza FP, indicating that the CoV FP exhibits a mechanistically different behavior. Membrane-ordering effects are greater and penetrate deeper into membranes when FP1 and FP2 act in a concerted manner, suggesting that they form an extended fusion "platform."

Introduction

Membrane fusion between viral and host membranes is a critical step during infection of enveloped viruses [1,2]. Because viral fusion is one of the first required steps of an enveloped virus infection, preventing it constitutes an attractive approach for the development of novel antiviral therapies. Viral membrane fusion also serves as a model for studying biological membrane fusion systems because of its relative simplicity. Compared to the more complex cellular synaptic vesicle membrane fusion system, which involves several proteins, only one type of glycoprotein, the viral fusion protein, is involved in the viral fusion process. For this reason, study of viral membrane fusion allows a focus on protein–lipid interactions and on biophysical aspects of the lipid bilayer during this process.

Coronaviruses (CoVs) are a diverse group of enveloped viruses that infect humans and animals, with several recent examples of zoonotic transmission, including severe acute respiratory syndrome CoV (SARS-CoV) and more recently Middle East respiratory syndrome CoV (MERS-CoV). Entry of CoVs into host cells is mediated by the viral spike (S) protein, which mediates both receptor binding (via the S1 domain) and membrane fusion (via the S2 domain). The S protein is categorized as a class I viral fusion protein, which includes the prototype envelope glycoprotein influenza hemagglutinin (HA) and the HIV envelope protein. However, the CoV S differs in several aspects from prototypical class I viral fusion

proteins. While influenza virus and HIV envelope proteins are known to be activated via cleavage by host cell proteases, this occurs at a single, restricted site directly adjacent to the fusion peptide (FP). In contrast, CoVs typically have two distinct cleavage sites that can be activated by a much wider range of proteases, with the FP function being able to be modulated by changes in the cleavage site position relative to the FP. This gives CoVs unique flexibility in the ability to invade new cell types, tissues, and host species. Several segments located in proximity with the heptad repeats (HR) region and transmembrane domain of the S2 domain of the SARS-CoV S protein have been proposed and characterized as putative CoV FPs [3–7]. The main objective of this work is to identify and characterize the *bona fide* CoV FP based on structural and functional analyses of peptide–lipid membrane interactions, using SARS-CoV S as a prototype. We have chosen SARS-CoV S as a model since most functional data are available with this virus. However, the FP is highly conserved across the very diverse CoV family, and so our findings would be directly applicable to all CoVs, including MERS-CoV as well as any novel viruses that are yet to emerge from their animal reservoir.

Glycoprotein-mediated viral entry into host cells requires an FP, the domain of the protein that interacts with opposing cellular membranes that is relatively hydrophobic in nature. However, identification of viral FPs is often difficult. While there are no universal definitions, FPs are generally fusion protein domains that insert into host membranes after proteolytic cleavage exposure and major conformational changes of the envelope glycoprotein, thus facilitating the initialization stage of membrane fusion. The flanking region of some FPs can also interact with membranes and have been shown to play an important role in the later stages of membrane fusion. Whether those flanking regions can be classified as FPs is still disputed. Also, the exact size of FPs is a matter of debate. For example, the length of the influenza FP is estimated to be 20 or 23 amino acids (aa), depending on the group that has characterized it [8–10].

The identification of the location of the FP for the CoV S protein is particularly challenging because of the large size of the fusion protein and the presence of multiple cleavage sites. For SARS-CoV S, the S1/S2 cleavage site is located at residue R667 (R: arginine), and the S2′ site is found at the R797 position [11]. Within the S2 fusion domain of SARS-CoV S protein, several regions have been proposed as FPs. These have been proposed based mainly on their hydrophobic amino acid content, and without functional experimental back-up. Using Wimley and White interfacial hydrophobicity analysis and peptide library scanning approaches, it has been suggested that the sequence corresponding to residues 770–788, located upstream of the S2′ cleavage site, is a putative FP (AltFP1) and that the sequence composed of residues 873–888, found upstream of the HR1 heptad repeat region, forms an "internal" FP (IFP or AltFP2) [3,4,7]. In addition, a region located proximal to the transmembrane region, the pre-transmembrane region or PTM (aa 1185–1202) was also found to have membrane-interacting properties [3,4]. It has been suggested that these segments within S2 work in concert to mediate the different steps of membrane fusion [4]. Most recently, these alternate protein segments have been subjected to structural characterization by NMR [and in some cases by electron spin resonance (ESR) and differential scanning calorimetry] [12,13]. The "FP" and "IFP" regions as defined by Mahajan and Bhattacharya have an uncertain functional role. Importantly, they show only limited sequence homology across the *Coronaviridae*, which would be very unusual for a viral FP. However, we have shown in previous functional experiments that the sequence immediately downstream of the S2′ site (798–815, FP1) is extremely well conserved among CoVs and possesses many features of a viral FP [14].

Recently, the structures of S proteins of several CoVs, such as murine hepatitis virus (MHV), human CoVs (HCoV) HCoV-HKU1 and HCoV-NL63, SARS-CoV, and MERS-CoV, have been revealed by cryo-electron microscopy [15–20]. These structural studies show that the CoV S regions corresponding to FP1 of SARS-CoV S are exposed at the surface of the corresponding S proteins. These structures have generally been interpreted such that FP1 is the viral FP. However, for all determined structures, the S protein is in its pre-fusion state and often have cleavage sites modified to promote protein stability of the recombinantly expressed protein. As such, there is currently limited information on the structural features of the CoV FP after proteolytic processing at S2′ and when interacting with lipid bilayers.

The insertion of FP into host lipid bilayers has been shown to be critical for viral fusion to occur as this event perturbs membrane structure. ESR spectroscopy is a powerful way to characterize FPs. We have successfully used ESR to study membrane structure modifications by insertion of various FPs, and consistently found that the FPs of HIV, influenza, and Dengue virus induce membrane ordering, that is, bilayer lipids becoming more ordered when the FP interacts with membranes [21–25]. We also found as a control that non-fusogenic mutants of the respective FPs have a much reduced ordering effect on membranes [21–25]. Membrane ordering is critical for membrane fusion, as it reflects the dehydration effect, which removes the repulsive force between the opposing membranes and allows them to come into a proximal position before fusion can take place [23,26]. Therefore, our approach provides a robust and reliable method to identify *bona fide* FPs. In this work, we have used this innovative approach to identify and characterize the CoV FP.

Using ESR to study CoV FPs, we found in the present work that the sequence immediately after the

S2′ (R797) cleavage site (FP1) increases membrane order. We also discovered that the sequence downstream of FP1 (FP2) also has characteristics of an active fusion domain. In addition, our results show that FP1 and FP2 work cooperatively as a bipartite fusion "platform" within an extended FP (FP1_2). In the presence of calcium ions, both FPs showed stronger membrane ordering, which is consistent with our observations that both FPs exhibit strong calcium dependencies for their membrane fusion function as assessed by isothermal titration calorimetry (ITC). Finally, our *in vitro* data are consistent with *in vivo* assays showing the dependence of calcium cations for SARS-CoV S-mediated virus entry and fusion. Together, our work provides a comprehensive analysis and strongly indicates that FP1_2 has the key characteristics of a *bona fide* FP, with unique properties.

Results

Design of peptides used for biophysical analyses

Viral FPs typically have low sequence conservation among different viral groupings. However, they are very well conserved within a given virus family. We have previously demonstrated that the SARS-CoV S region immediately downstream of the S2′ cleavage site (SFIEDLLFNKVTLADAGF, referred to as FP1 here) was highly conserved among CoVs [14]. Furthermore, we have also shown that a pair of highly conserved cysteines (C822–C833) found downstream of FP1 is essential for the membrane fusion function along with core-associated residues D830 and L831 (the region downstream of FP1 and containing these residues is referred to as FP2 here) [5]. To validate these findings with more recent sequence information, we first performed a comprehensive protein sequence alignment analysis (Fig. 1a) of the extended region corresponding to the FP1_2 fusion domain of SARS-CoV. These results are summarized in the Weblogo generated using the sequence alignment data (Fig. 1b). The location of the FP1_2 segment in the context of a model structure of the SARS-CoV S protein monomer, which is based on MHV S structure, is highlighted in Fig. 1c. The analysis confirms and extends our earlier findings to all four characterized CoV genera with six invariant and eight highly conserved sites. Among the highly conserved and invariant sites is the LLF motif and the conserved cysteine pair previously found to be critical for membrane fusion by site-directed mutagenesis and functional assays [5,14].

Next, to perform biophysical analyses, peptides corresponding to the SARS-CoV amino acid regions 798–818 (FP1) and 816–835 (FP2) were synthesized, along with an extended FP corresponding to the 798–835 region (FP1_2) (Fig. 1d). Alanine substitutions in the LLF motif of FP1 were shown to be fusion defective in our previous study, and so a LLF→AAA modified peptide was also generated [14]. Other peptides previously proposed to be CoV FPs were synthesized, including an "N-terminal FP" that is immediately downstream of the SARS-CoV S1/S2 cleavage site (770–788, AltFP-A) and an internal FP (873–888, IFP or AltFP-B), as well as a negative control peptide that corresponds to the region downstream of IFP within the HR1 region (887–904, HRP). The synthesized FPs contain a C-terminal GGGKKKK hydrophilic tag sequence except HRP and FP1_2. The GGGKKKK tag sequence is used to increase the solubility of the peptides. This approach has been applied to other FPs previously and has been shown to have no effect on the function of FPs [24,27,28]. Here, in order to further demonstrate that it does not interfere with our ESR measurements on FP1, we synthesized a variant FP1 (pFP1) devoid of the C-terminal GGGKKKK tag. We also synthesized randomized sequence variants of FP1 and FP2 (rFP1 and rFP2, respectively), which have the same amino acid composition as FP1 and FP2 but with a shuffled arrangement of residues.

We used 1-palmitoyl-2-oleoyl-sn-glycero-3-phosphocholine (POPC)/1-palmitoyl-2-oleoyl-sn-glycero-3-phosphoserine (POPS)/cholesterol (Chol) = 3/1/1 as the model membrane system. PS is an anionic lipid that is found in the inner leaflet of the cytosolic membrane and to some extent in endosomal membranes [29]. It is critical for synaptic membrane fusion [30–32], and it also promotes viral entry of various viruses [33,34]. A recent study showed that PS is critical for HIV entry [35]. Moreover, PS has been widely used in FP research [36,37] and is also consistent with the system that we have used previously [14]. We used multilamellar vesicles (MLVs) in our ESR study as they can be much more concentrated than small unilamellar vesicles (SUVs) and greatly enhance the ESR signal. Furthermore, the use of MLVs is consistent with our previous studies [23–25].

FP1 increases membrane ordering

The ESR signal of the spin labels on the lipids in membrane bilayers is sensitive to the local environment. Three spin labels were used: dipalmitoylphosphatidyl-tempo-choline (DPPTC) has a tempocholine headgroup and the spin is sensitive to changes of environment at the headgroup region; 5PC and 14PC have a doxyl group in the C5 or C14 position of the acyl chain, respectively (Fig. 1e), and they are sensitive to the changes of environment in the hydrophobic acyl chain region at different depths. Using the NLSL program based on the microscopic order macroscopic disorder model (MOMD) [38,39], the order parameter of the spin can be extracted, which

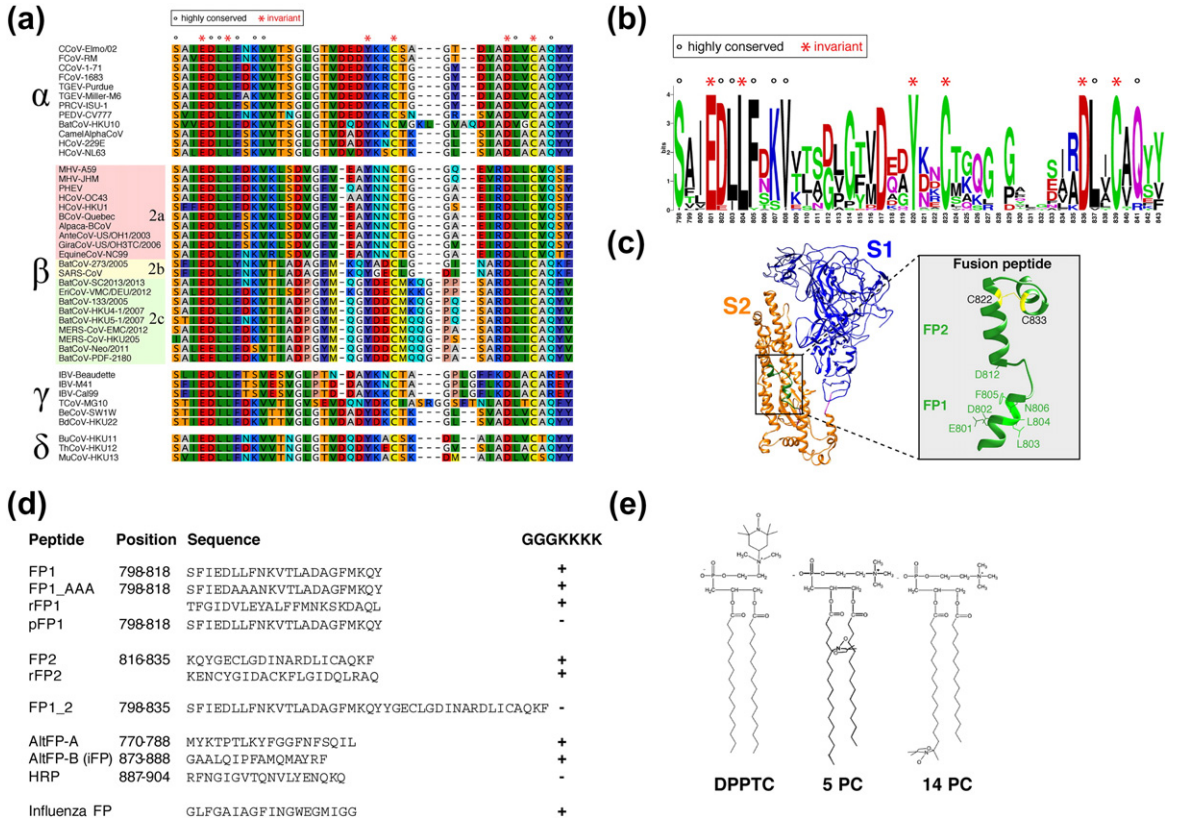

Fig. 1. (a) Protein sequence alignment of CoV FP region. The sequences of 42 representative alpha-, beta-, gamma-, and deltacoronavirus spike proteins were aligned using MUSCLE within the Geneious software suite, and the aligned region corresponding to the SARS-CoV FP1 and FP2 was extracted. (b) Weblogo representation of the CoV spike (S) region downstream of the S_2' cleavage site for all four CoV genera (FP1_2 region) showing conserved and variable residue positions. Sequence conservation of the region corresponding to the SARS-CoV aa 798–843 was represented using above-mentioned alignment data and Weblogo 3.0. Numbering corresponds to SARS-CoV S sequence. c. Location of the FP1_2 segment in the context of the SARS-CoV S monomer, highlighting key residues. The structural model of SARS-CoV S was based on the MHV S structure (PDB: 3JCL) using the Modeller comparative modeling tool in Chimera software. (d) Peptides used in this study. (e) Structure of spin-labeled lipids used in this study.

is correlated with the order of the membrane. Thus, the effect of peptide binding on the structure of the membrane can be monitored. These three spin-labeled lipids have been used in previous studies and their ability to detect changes in membrane structure has been validated [26,40]. Our previous studies examined the effect of a various viral FPs, including those of influenza virus [21,23], HIV [24], and Dengue virus [25], as well as the FP of the ancestral eukaryotic gamete fusion protein HAP2 [25]. All of these peptides were found to induce membrane ordering in the headgroup region as well as in the shallow hydrophobic region of bilayers (i.e., 5PC).

As shown in Fig. 2a, in the MLVs composed of POPC/POPS/Chol = 3/1/1, when the peptide:lipid ratio (P/L ratio) of FP1 increases from 0 to 2 mol%, the order parameter S_0 of DPPTC increases significantly from 0.44 to 0.48 at pH 5. The increase of the S_0 is similar to the effect of influenza FP as we have previously shown [23]. However, this ordering effect is slightly reduced at pH 7 (0.44 to 0.46). The membrane order of 5PC also significantly increases from 0.51 to 0.58 at pH 5 when FP1 concentration increases; its increase in the pH 7 condition is similar (Fig. 2b). The interaction of FP1 with lipid bilayers has virtually no effect on the S_0 of 14PC (Fig. 2c) regardless of pH.

Individual alanine mutations within the LLF motif of FP1 have been shown previously to abrogate fusogenicity of the SARS-CoV S protein based on *in vivo* experiments, and an LLF➔AAA variant FP was unable to mediate liposome fusion in lipid mixing assays [14]. As shown in Fig. 2d and e, FP1_AAA has no effect on the membrane ordering for all three spin label positions. Thus, the membrane-ordering effect of FP1 we observed with ESR is in good agreement with previously determined functional fusogenicity data. To further validate that the membrane-ordering effect of FP1 we detect is not artificial, a randomized peptide (rFP1), which has the same amino acid composition

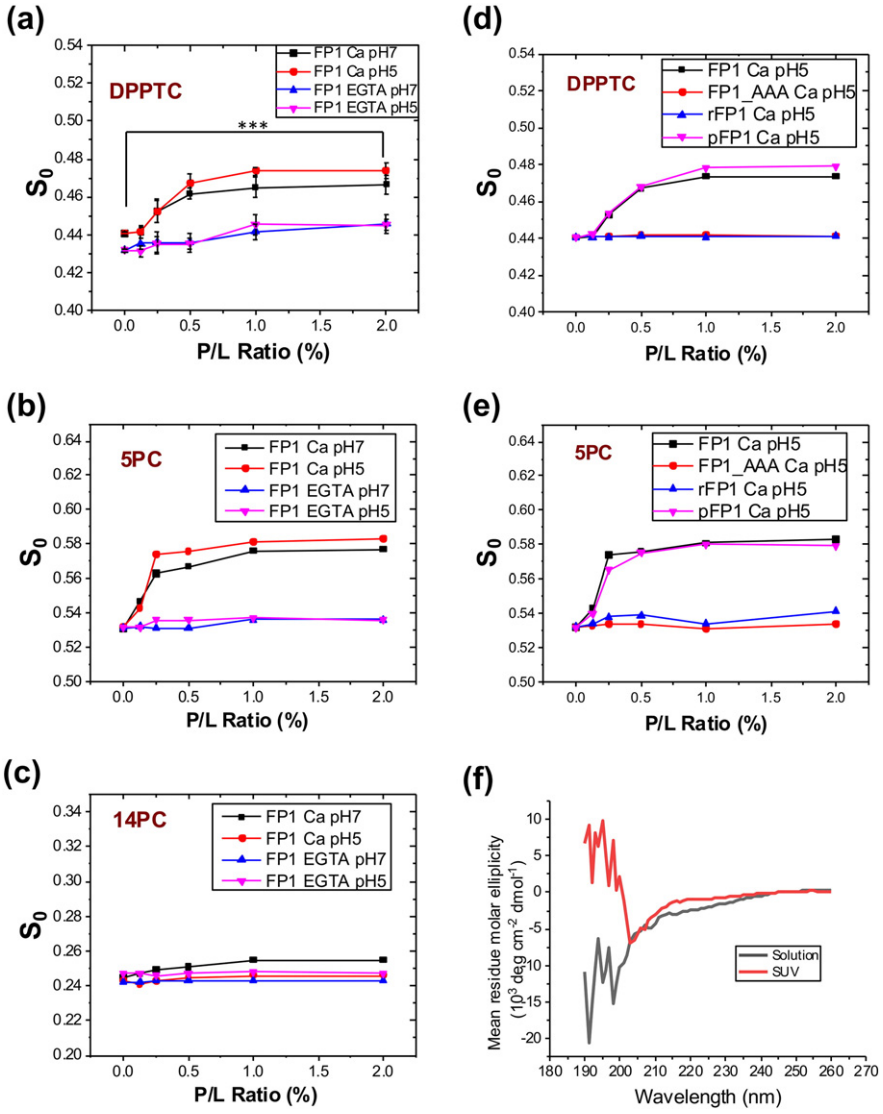

Fig. 2. (a–c) Plots of order parameters of DPPTC (a), 5PC (b), and 14PC (c) *versus* peptide:lipid ratio (P/L ratio) of SARS FP1 in POPC/POPS/Chol = 3/1/1 MLVs in buffer with 150 mM NaCl at 25 °C. Black, 1 mM Ca^{2+} and at pH 7; red, 1 mM Ca^{2+} and at pH 7; blue, 1 mM EGTA and at pH 7, and purple, 1 mM EGTA and at pH 5. (d–e) Plots of order parameters of DPPTC (d) and 5PC (E) *versus* P/L ratio in POPC/POPS/Chol = 3/1/1 MLVs in pH 5 buffer with 150 mM NaCl at 25 °C. Black, FP1; red, FP1_AAA; blue, rFP1; and purple, pFP1. The experiments were typically repeated two to three times. The typical uncertainties found for S_0 ranges from 1 to 5 × 10^{-3}, while the uncertainties from repeated experiments were 5–8 × 10^{-3} or less than ±0.01. We show in panel A the bars for SD. Statistical significance analyses were performed using two-tailed Student's *t*-test on the S_0's of 0% FP1 and 2% FP1 at the "Ca pH 5" condition, *** ≤ 0.001, highly significant. (F) CD Spectra of FP1 in solution (black) and POPC/POPS/Chol = 3/1/1 SUVs in pH 5 buffer at 25 °C.

as FP1 but with a shuffled sequence, was synthesized and its effect on lipid bilayer order was measured. As shown in Fig. 2d and e, it has little to no effect on the membrane order, indicating that the primary and secondary structures of FP1 are critical for membrane interactions.

To understand whether the hydrophilic C-terminal tag sequence GGGKKKK affects membrane ordering and/or prevents the N-terminus of FP1 from inserting deeper into the membrane, we synthesized the GGGKKKK sequence alone and a variant FP1 without GGGKKKK (pFP1). Without GGGKKKK, pFP1 is no longer soluble in water. Thus, we pre-mixed the desired amounts of pFP1 with lipids in chloroform with P/L ratios from 0% to 2%, and then made the MLVs with pFP1 inserted. The resulting S_0 from the spectra shows that pFP1 has a very similar membrane-ordering effect profile to FP1 (Fig. 2d and e). Thus, the GGGKKKK

sequence does not appear to interfere with the membrane ordering induced by FP1. Control experiments with the GGGKKKK hydrophilic tag alone show that it cannot induce membrane ordering (data not shown). These combined results indicate that FP1 induces membrane ordering in the headgroup and shallow hydrophobic regions.

The formation of secondary structures is critical for the activity of FP1

We used circular dichroism (CD) spectroscopy to examine the secondary structures of the peptides in solution and in membranes, which allows us to monitor the structural transitions occurring between these two environments. As shown in Fig. 2f, while FP1 exhibits mostly a random coil structure in solution, it changes into a mixture of alpha-helix, beta-sheet, and random-coil structures in the presence of SUVs composed of POPC/POPS/Chol = 3/1/1 at pH 7. Here, the reason we used SUVs instead of MLVs is that MLVs are too big for CD spectroscopy, which would cause scattering and a noisy signal. The CD spectra of FP1 at pH 5 are similar to those observed for the pH 7 condition (not shown). In contrast, the fusion defective variant FP1_AAA exhibits a mostly random-coil structure in both solutions with or without the presence of SUVs. Thus, when interacting with lipid bilayers, FP1 adopts a secondary structure that differs from the one in solution, a result that suggests that the structural transition is an important factor for its activity.

The region downstream of FP1 (FP2) also induces membrane ordering

Our previous study has shown that a domain containing a conserved pair of cysteines found downstream of FP1 (C822 and C833), along with other residues (D830, L831), plays an essential functional role for S-mediated fusion [5], which indicates that this region may contribute to membrane fusion. We designated the sequence from aa 816–835 as FP2 and studied its possible involvement in membrane-ordering effects.

As shown in Fig. 3, we observed that FP2 also increases membrane ordering. When the P/L ratio

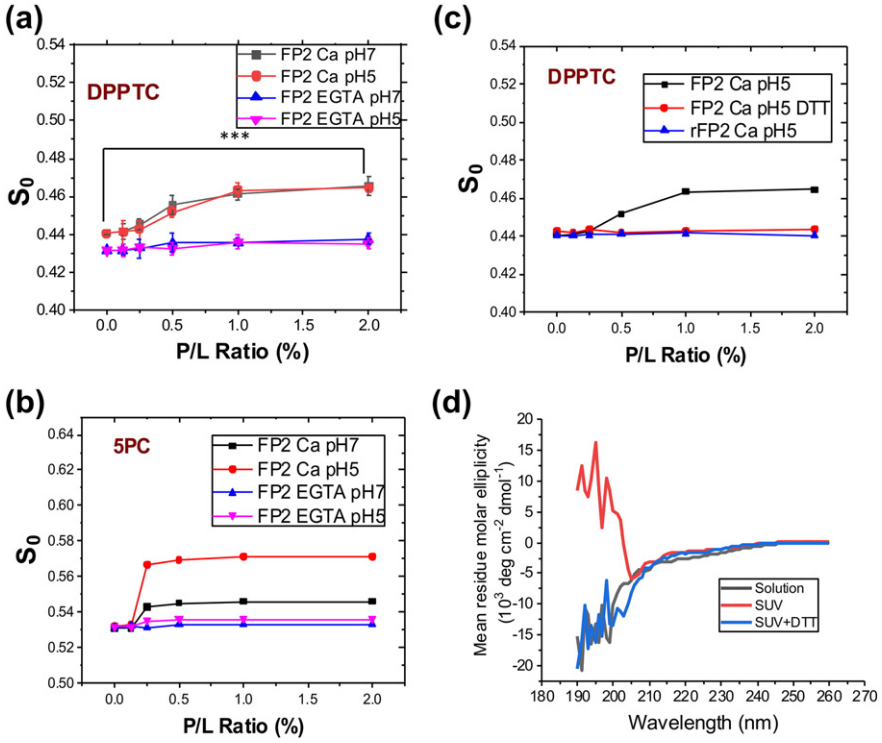

Fig. 3. (a–b) Plots of order parameters of DPPTC (a) and 5PC (b) *versus* P/L ratio of SARS FP2 in POPC/POPS/Chol = 3/1/1 MLVs in buffer with 150 mM NaCl at 25 °C. Black, 1 mM Ca^{2+} and at pH 7; red, 1 mM Ca^{2+} and at pH 7; blue, 1 mM EGTA and at pH 7, and purple, 1 mM EGTA and at pH 5. (c) Plot of order parameters of DPPTC *versus* SARS FP2 concentration in POPC/POPS/Chol = 3/1/1 MLVs in pH 5 buffer at 25 °C. Black, FP2 without DTT, red, FP2 with 5 mM DTT; blue, rFP2. The experiments were typically repeated two to three times. The typical uncertainties found for S_0 range from 1 to 5 × 10^{-3}, while the uncertainties from repeated experiments were 5–8 × 10^{-3} or less than ±0.01. We show in panel A the bars for SD. Statistical significance analyses were performed using two-tailed Student's *t*-test on the S_0's of 0% FP2 and 2% FP2 at the "Ca pH 5" condition, *** ≤ 0.001, highly significant. (d) CD spectra of FP1 in solution (black), POPC/POPS/Chol = 3/1/1 SUVs (red) and in SUVs with 5 mM DTT (blue) in pH 5 buffer at 25 °C.

increases from 0 to 2% mol:mol, the S_0 of DPPTC spin labels increases significantly from 0.44 to 0.46 at pH 5. The S_0 of 5PC is also increased from 0.51 to 0.57 at pH 5; the increase of S_0 of 5PC is smaller at pH 7 for reasons that are unclear. FP2 has no effect on the S_0 of 14PC (not shown). As in the FP1 case, we also synthesized a randomized peptide (rFP2), which has the same amino acid composition as FP2 but with a shuffled sequence, and its effect on lipid bilayer order was measured. As shown in Fig. 3c, rFP2 has little to no effect on the membrane order.

Two cysteines (C822 and C833) within FP2 are considered to form an internal disulfide bond, giving this domain a loop structure [5]. We tested whether such a disulfide bond could play a role in the FP2-mediated membrane ordering. We found that in the presence of 5 mM dithiothreitol (DTT), a reducing agent that removes disulfide bonds, the membrane-ordering effect of FP2 was abrogated (Fig. 3c). Thus, the activity of FP2 is dependent on the formation of the internal disulfide bond. From CD spectroscopy analysis, we found that the presence of 5 mM DTT significantly changes the secondary structure of FP2 in SUVs, as the spectrum of FP2 in the presence of SUVs and DTT is similar to the spectrum of FP2 in solution (Fig. 3d). The result suggests that the disulfide bond ensures a proper folding of FP2, which is essential for its function on membrane ordering.

Enthalpy changes of FP–membrane interactions

The importance of correct peptide folding can be further analyzed by comparing membrane binding enthalpies of FPs as measured by ITC. In this experiment, small amounts of peptide were injected into a reaction cell containing a large excess of SUVs. Thus, during the whole titration process, the amount of available membrane can be regarded as constant, and all injected peptides can be regarded as binding to the membranes. As a result, the reaction heat in each injection is equal. The enthalpy of reaction can be calculated from the average of heat in each injection [27,41].

When the enthalpy change of the GGGKKKK is subtracted, the $\Delta\Delta H$ of FP1 is −14.8 kcal/mol, and the $\Delta\Delta H$ of FP2 is −11.6 kcal/mol, while FP1_AAA exhibits very little enthalpy change (−5.66 kcal/mol) (Table 1). FP–membrane interactions are usually enthalpy-driven [42], indicating that the driving force of the FP–membrane interactions is the formation of secondary structures in the membranes, other than the entropy gained by hydrophobic interactions. Thus, the greater binding enthalpy indicates a better transition of secondary structures. These ITC results are consistent with our CD and ESR experimental data.

AltFP-A and AltFP-B induce membrane ordering less efficiently

It has been suggested that the peptide located C-terminally of the S1/S2 cleavage site (aa 770–788, AltFP-A) and an "internal" FP (873–888, AltFP-B) are putative FPs. A study was conducted by Basso and colleagues [12] using ESR measurements similar to the ones used in this work. The authors showed a noticeable change of S_0 in MLVs composed of DPPG, DPPS, or POPA at 5 mol% of both peptides. However, the conditions used in that work do not match physiological conditions in two key aspects: (1) the concentration of peptides used was high and (2) the membrane contains 100% charged phospholipids and lacks Chol, a mixture that does not correspond to physiological settings. In addition, neither peptide consistently increases membrane order; that is, the authors observed a decrease in membrane order in some conditions.

We synthesized both peptides and tested them using our lipid system, which, like other systems widely used in FP research, has 20% charged lipid [36,43–45]. As shown in Fig. 4, although both

Table 1. Thermodynamic parameters measured using ITC

A. Binding enthalpy of FPs to POPC:POPS:Chol = 60:20:20 SUVs at 37 °C. ΔH was averaged from two repeats and thirty data points. $\Delta\Delta H = \Delta H$(FPs) − ΔH(GGGKKKK).

Peptide	ΔH (kcal/mol)	$\Delta\Delta H$ (kcal/mol)
GGGKKKK	−9.60 ± 0.12	N.A.
FP1	−24.40 ± 0.16	−14.80
FP1_AAA	−15.26 ± 0.18	−5.66
FP2	−21.21 ± 0.23	−11.61

B. Interaction between Ca^{2+} cations and the FPs measured at 37 °C, averaged from two repeats. ΔH, K_b, and n were calculated from the fitting using the one-site model. ΔG and $-T\Delta S$ were calculated from ΔH and K_b.

Peptides	ΔH (kcal/mol)	K_b ($\times 10^4$ M^{-1})	n	ΔG (kcal/mol)	$-T\Delta S$ (kcal/mol)
FP1	4.67 ± 0.31	3.76 ± 0.51	0.92 ± 0.04	6.49	−1.80
FP2	5.94 ± 0.27	2.34 ± 0.13	1.02 ± 0.02	6.20	−0.26
FP1_2	6.77 ± 0.45	2.49 ± 0.35	1.70 ± 0.04	6.23	0.54

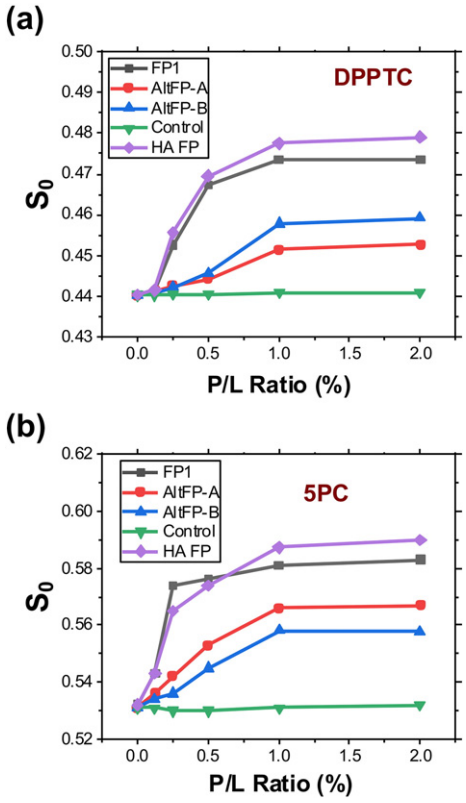

Fig. 4. (a–b) Plots of order parameters of DPPTC (a) and 5PC (b) *versus* P/L ratio in POPC/POPS/Chol = 3/1/1 MLVs in buffer with 150 mM NaCl and 1 mM $CaCl_2$ at 25 °C. Black, FP1; red AltFP1; blue, AltFP2; green, Control; purple, influenza HA FP.

AltFP-A and AltFP-B increase membrane order of DPPTC and 5PC spin-labeled lipids, the effect is smaller than those seen for FP1 in two ways. First, the maximum changes of S_0 of both DPPTC and 5PC for AltFP-A (0.012 and 0.036, respectively) and AltFP-B (0.019 and 0.027, respectively) are smaller than those for FP1 (0.033 and 0.051, respectively). Second, when we fitted the S_0-P/L ratio curve with a sigmoidal curve, the concentration of peptide that induces half of the maximal ΔS_0 could be determined. For FP1, these concentrations for DPPTC and 5PC are 0.39% and 0.22%, respectively, which are significantly lower than those for AltFP-A (0.77% and 0.52%, respectively) and AltFP-B (0.75% and 0.58%, respectively). The results indicate that FP1 has a significantly higher activity than the other two peptides. Interestingly, we could not observe the change of S_0 of 14PC (not shown) for all peptides, although Basso *et al.* showed that the S_0 of 16PC was affected by both AltFP-A and AltFP-B in their 100% charged membranes. FPs of influenza virus and HIV insert into the membranes in a shallow manner, with no effect on 14PC spin-labeled lipids [21,24]. Our results with the SARS-CoV FP1 show that it has a consistently higher membrane-ordering activity than AltFP-A and AltFP-B, suggesting that FP1 is more likely a *bona fide* FP. Furthermore, our biophysical data are in agreement with our previous sequence and functional analyses showing that conserved residues within FP1, particularly the LLF motif, are critical for membrane fusion [14].

The SARS-CoV FP-induced membrane ordering is calcium dependent

Our initial ESR measurements (Figs. 2 and 3) showed that adding 1 mM of the chelating agent EGTA effectively abrogates membrane-ordering effects of FP1 and FP2. We thus studied in more detail the effects of calcium on membrane fusion. We examined whether trace Ca^{2+} cations in solution may have any effects on POPC/POPS/Chol membranes. We compared the order parameter S_0 of samples in the presence of 1 mM EGTA, without EGTA or Ca^{2+}, and in the presence of 1 mM Ca^{2+}. Analysis of these different conditions shows that trace Ca^{2+} ions increase membrane order of the headgroup (DPPTC) noticeably but have no effects on acyl chains (5PC and 14PC, data not shown). This is likely because Ca^{2+} cannot penetrate into the hydrophobic layer of the membranes.

In order to test the effects of Ca^{2+} on FP-inducing membrane ordering, we maintained the concentration of FP at a constant 1 mol% P/L ratio and measured the order parameter S_0 with increasing calcium concentrations from 0 to 2.0 mM (Fig. 5a); the highest calcium concentration used here is higher than the extracellular concentration of Ca^{2+} in human adult lungs (about 1.3 mM) [46]. The increase in S_0 has two sources, the FPs and the Ca^{2+}; thus, we generated a ΔS_0-Ca^{2+} concentration plot, where $\Delta S_0 = S_0$ (membrane with 1% FP) – S_0 (membrane without FP) at each Ca^{2+} concentration. This subtraction cancels the membrane ordering induced by Ca^{2+} only, with the ΔS_0 at each Ca^{2+} concentration representing only the contributions of the FPs. As shown in Fig. 5a, Ca^{2+} increases the ΔS_0 of both FP1 and FP2. As a control, influenza virus FP was also analyzed and did not show any calcium dependency on membrane ordering.

Interactions of FPs with calcium cations detected by ITC

We used ITC to investigate whether Ca^{2+} cations directly interact with SARS-CoV FPs. During titration, a total of 300 μL 2 mM $CaCl_2$ in a pH 5 buffer (with 10 μL solution in each injection) was injected into a reaction cell containing 1 mL of FPs at 0.4 mM. The background caused by the dilution of $CaCl_2$ has been subtracted by using data from a control experiment that titrated $CaCl_2$ in a pH 5 buffer. Substantial heat absorbed during the titration was observed, with the heat absorbed saturating toward the end of the

titration. As shown in Fig. 5b and Table 1B, when the heat *versus* molar ratio plot was fitted using a one-site model that assumes that all binding sites have the same binding affinity, we calculated the enthalpy change $\Delta H = 4.67$ kcal/mol, with binding constant $K_b = 3.76 \times 10^4\ M^{-1}$ and stoichiometry $n = 0.92$. From these parameters, we further calculated the free energy change $\Delta G = -RT\ln K_b = 6.49$ kcal/mol and $-T\Delta S = \Delta G - \Delta H = -1.80$ kcal/mol. The data show that the calcium–FP1 interaction is endothermic, and the binding ratio is one calcium per peptide. The reason for the endothermic reaction could be because the buffer solution (150 mM NaCl) contains significant amounts of Na^+ ions that could also interact with FP1 and that a stronger binding of Ca^{2+} cations displaces bound Na^+ into the bulk solution. To test this hypothesis, we reduced the NaCl concentration to 50 mM and performed an ITC titration. However, the baselines of the titration curves we obtained were unstable, and we could not extract meaningful data. The reason for this result is unclear, but it is possible that the peptide requires a certain level of salt concentration to maintain its structure. We performed the same experiment with FP2 and FP1_2 (Fig. 5c and d). As shown in Fig. 5c and Table 1B, like FP1, FP2 also exhibits an endothermic reaction with Ca^{2+}, with a stoichiometry of $n = 1.02$, $\Delta H = 5.94$ kcal/mol, and $K_b = 2.34 \times 10^4\ M^{-1}$. Furthermore, in the case of FP1_2, the stoichiometry is $n = 1.70$. The ITC experiments we conducted demonstrate strong evidence for direct calcium–FP interactions, with one Ca^{2+} cation binding per FP1 or FP2.

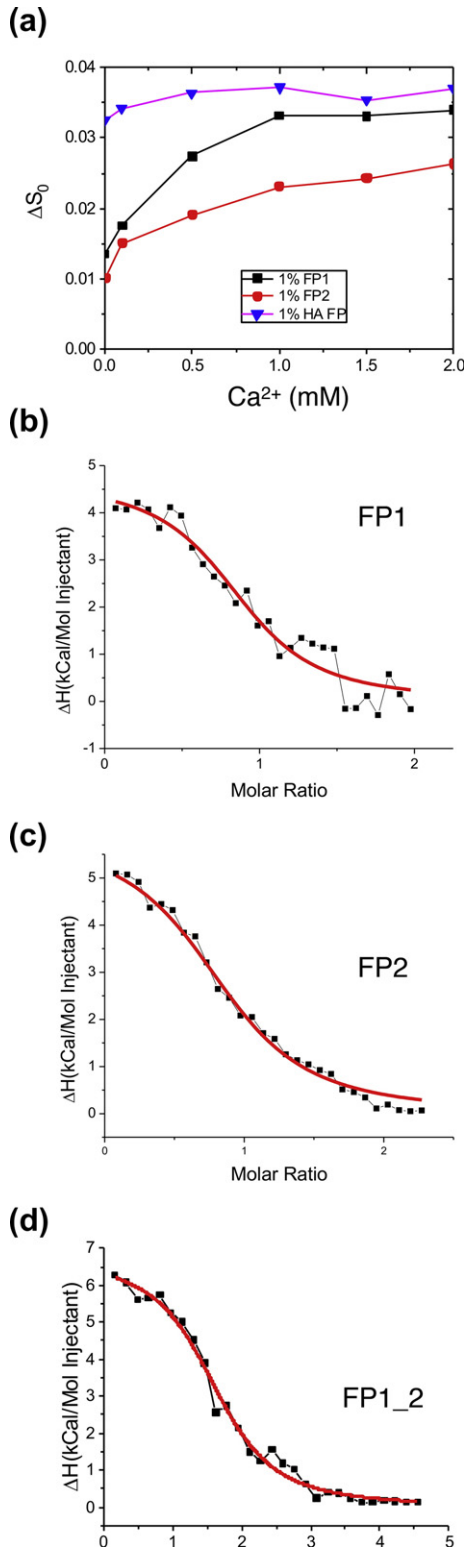

Fig. 5. (a) Plot of different of order parameters of DPPTC with and without 1% peptide binding (ΔS_0) versus Ca^{2+} concentration in POPC/POPS/Chol = 3/1/1 MLVs in buffer with 150 mM NaCl at 25 °C. Black, FP1; red, FP2; purple, influenza HA FP. (B–D) ITC analysis of Ca^{2+} binding to FP1 (b), FP2 (c), and FP1_2 (d). The peptides were titrated with $CaCl_2$. The integrated data represent the enthalpy change per mole of injectant, ΔH, in units of kcal/mol as a function of the molar ratio. Data points and fitted data are overlaid.

Calcium is important for membrane fusion in live cells

To assess the functional role of calcium cations during SARS-CoV S-mediated fusion and viral entry, we performed pseudotyped particle infectivity assays. We generated murine leukemia virus pseudotyped viruses harboring full-length SARS-CoV S envelope glycoproteins and containing the luciferase reporter gene. These viral particles are pertinent surrogates of native enveloped viruses, as they recapitulate all entry steps governed by the heterologous (SARS-CoV S) fusion protein and allow for a quantitative measurement of infectivity thanks to the luciferase reporter expressed only in an infected cell [47]. We first performed an extracellular calcium ion depletion experiment in which Vero-E6 cells were washed with phosphate buffer saline (PBS) with or without calcium ions, incubated with culture medium with or without

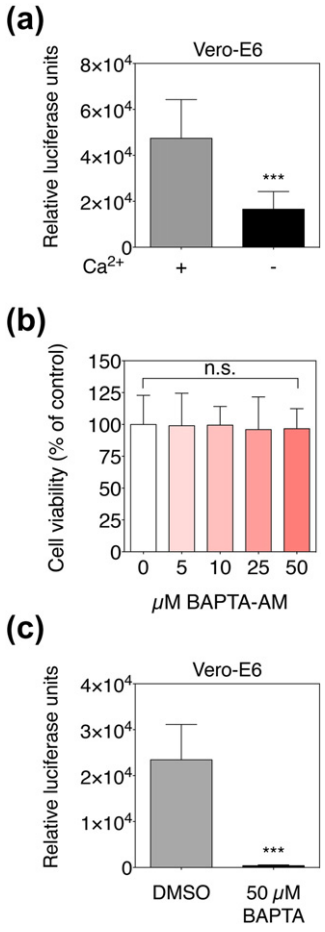

Fig. 6. Effect of Ca^{2+} cation depletion on SARS-CoV S-mediate cell entry. (a) Effect of extracellular Ca^{2+} cation depletion on SARS-CoV S pseudotyped particle entry. Murine leukemia virus-luciferase pseudotyped particles harboring the SARS-CoV S protein (SARSpp) were used to infect African green monkey kidney Vero-E6 cells in absence (–, 0 mM) or presence (+, 1.8 mM) of Ca^{2+} ions. Seventy-two hours post-infection, cells were assayed for luciferase activity using a luminometer. (b) Cell viability assay of Vero-E6 cells treated with increasing concentrations of the BAPTA-AM chelating agent. After treatment of cells with BAPTA-AM (0–50 μM), cell viability was measured using a luminescence-based ATP quantitation assay. Results are expressed as average cell viability (% of 0 μM condition, i.e., DMSO control), with error bars representing SD from the average of three independent experiments. Data were analyzed statistically using a two-tailed Student *t*-test with the following convention for *p*-value significance: not significant (n.s.), $p > 0.05$. (c) Effect of intracellular Ca^{2+} cation depletion using BAPTA-AM on SARS-CoV S-mediated entry. SARSpp pseudovirions were used to infect Vero-E6 cells that were pre-treated for 2 h with the intracellularly active Ca^{2+} chelator BAPTA-AM or DMSO (control). Seventy-two hours post-infection, cells were assayed for luciferase activity using a luminometer. For panels A and B, results are expressed as average relative luciferase units from three independent experiments, each performed in triplicates. Error bars indicate SD and statistical significance analyses were performed using two-tailed Student's *t*-test, *** ≤ 0.001, highly significant.

calcium ions, and infected with pseudovirions in the presence or absence of the chelating agent ethylenediaminetetraacetic acid (EDTA) (Fig. 6a). This assay shows that depletion of extracellular calcium cations significantly decreases SARS-CoV pseudotyped particle (SARSpp) infectivity, with a measured ~2.9-fold decrease. As SARS-CoV is known to enter cells through the endocytic pathway, we then tested the effect of 1,2-bis(2-aminophenoxy)ethane-*N*,*N*,*N*′,*N*′-tetraacetic acid tetrakis (BAPTA-AM), a calcium-specific cell membrane-permeable chelator, to investigate the role of intracellular calcium on SARS-CoV virus entry (Fig. 6b and c). We first assessed the effect of BAPTA-AM on cell viability (Fig. 6b). Increasing concentrations of BAPTA-AM were incubated with Vero-E6 cells, which were then analyzed for cell viability using luminescence-based ATP quantitation assay. This analysis shows that cell viability is not significantly impacted up to the highest concentration tested of 50 μM. Upon depletion of intracellular calcium ions in Vero-E6 cells using a similar 50 μM BAPTA-AM treatment to that mentioned above, we observed a remarkable ~60-fold decrease in SARSpp infectivity (Fig. 6c). Taken together, our functional assays strongly support an important functional role played by Ca^{2+} ions during viral fusion and entry of SARS-CoV.

Cooperation of FP1 and FP2 induces greater membrane-ordering effect

We have previously shown that the cooperativity between the influenza FP and the influenza transmembrane domain increases the membrane-ordering effect using ESR [23]. These findings indicated that two peptide segments work cooperatively to enhance membrane ordering. We examined the possible cooperative effects of FP1 and FP2 when they are present together with lipid bilayers. We mixed FP1 and FP2 at a 1:1 molar ratio before they were allowed to bind to the membranes. As shown in Fig. 7a and b, binding of the mixture of FP1 and FP2 at 1:1 ratio (Mix. of FP1 + FP2) was accompanied by a membrane ordering of DPPTC and 5PC at pH 5. When the same amounts of total peptide were compared, the mixture of FP1 + FP2 increases S_0 of DPPTC to 0.47 when the total P/L is 2% (i.e., 1% FP1 and 1% FP2), which is higher than the S_0 for the 2% FP1 or 2% FP2 individual conditions. Also, the 5PC membrane ordering increases for the mixture of FP1 + FP2 are more noticeable, up to 0.61 at 2% total P/L ratio. Interestingly, although the mixture of FP1 + FP2 has no effect on 14PC, it has a small but observable membrane-ordering effect on 10PC (from 0.32 to 0.34; Fig. 7c), which cannot be observed with FP1 or FP2 individually. Thus, the cooperativity of FP1 and FP2 not only allows for a greater membrane-ordering effect than the addition of FP1 or FP2 individually, but also enables a deeper reach within the lipid bilayer.

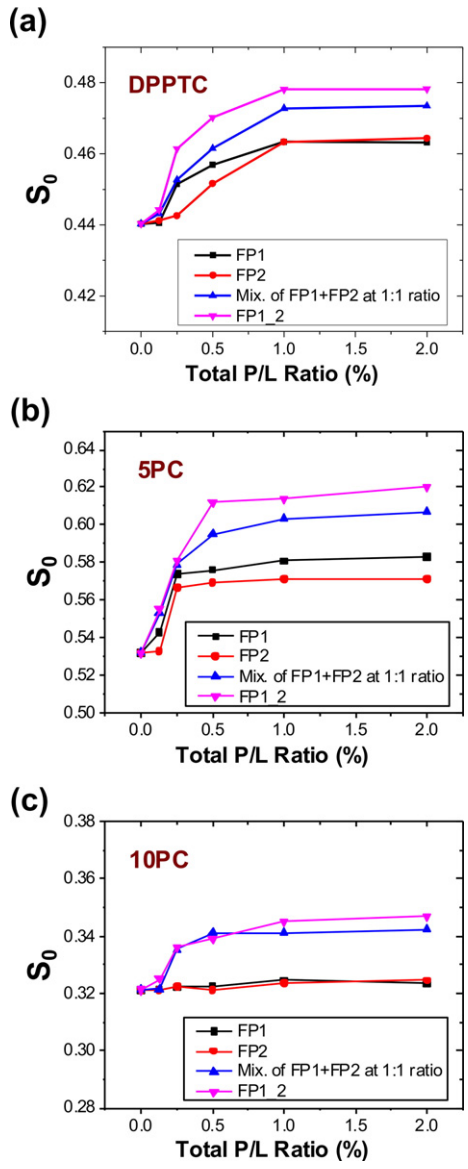

Fig. 7. Cooperative effect of FP1 and FP2. (a–c) Plots of order parameters of DPPTC (a), 5PC (b), and 10PC (c) *versus* total P/L ratio in POPC/POPS/Chol = 3/1/1 MLVs in buffer with 150 mM NaCl and 1 mM $CaCl_2$ at 25 °C. To make an accurate comparison, the actual total P/L ratio (mol:mol) of FP1_2 is half of its nominal value in the figures, because the molecular weight of FP1_2 is approximately double that of either FP1 or FP2 alone.

We synthesized an extended peptide (FP1_2), which is composed of the FP1 and FP2 linked together and without the GGGKKKK C-terminal tag sequence because the peptide could be readily dissolved in water without the hydrophilic tag. To make an accurate comparison, the actual total P/L ratio (mol:mol) of FP1_2 is half of its nominal value in Fig. 7, because the molecular weight of FP1_2 is approximately double that of either FP1 or FP2 alone. As shown in the figure, FP1_2 has a similar membrane-ordering effect to the mixture of FP1 + FP2, with a slightly greater ordering effect, possibly due to a better coordination between the FP1 and FP2 domains.

Discussion

The mechanism of membrane fusion is still only partially understood. Our previous work showed that the FPs of influenza virus, HIV, and Dengue virus induce increased membrane ordering in a collective fashion, that is, a significant increase in S_0 as a function of P/L ratio. We further suggested that FP-induced membrane ordering is a result of dehydration due to peptide insertion, which is a prerequisite step for removal of the repulsive forces between two opposing membranes and thereby facilitating initialization of membrane fusion [21–25]. Our current study extends these concepts to the CoV FP, focusing on the well-characterized SARS-CoV, and reveals several key new mechanisms of viral FP insertion.

We have shown that the previously identified SARS-CoV FP1 [14], found immediately downstream of the S2′ cleavage site, has a strong membrane-ordering effect on lipid headgroups and shallow hydrophobic regions of target bilayers. This observed membrane-ordering activity is correlated with the function of the FP, as the inactive LLF➔AAA mutant does not have such an effect. The membrane-ordering activity also depends on the correct amino acid sequence, because rFP1, which has the same residue composition as FP1 but in random order, does not induce membrane ordering. Correct folding of the peptide in the membrane is also an important parameter, as the LLF➔AAA mutant does not fold in the same way in the membrane as the FP1, as shown by CD spectroscopy and ITC. This finding is consistent with our previous studies on other viral FPs [21,24,25]. We further compared FP1's membrane ordering ability with those of two other proposed FPs AltFP-A and AltFP-B, and found that it has a higher activity than the other two. Our previous functional experiments on the SARS-CoV S protein suggest that FP1 possesses many features of an FP [14], and the recently published cryo-electron microscopy structures of the different CoV S proteins, including that of SARS-CoV S, suggest that in its pre-fusion state, FP1 appears to be exposed at the surface of the glycoprotein's S2 domain [15,19,20]. Taken together, these data indicate that FP1 is more likely a *bona fide* FP for the SARS-CoV S protein.

We have demonstrated that FP2 also exerts a membrane-ordering effect similar to that observed for FP1. The FP2 membrane-ordering activity is also dependent on correct folding, which is maintained by an internal disulfide bond, as addition of the reducing agent DTT eliminated membrane-ordering activity.

FP2 is important because the membrane-ordering activity is significantly enhanced when FP1 and FP2 function cooperatively. Together, they induce a greater ordering effect than FP1 and FP2 separately, and exhibit a deeper reach into the membrane. Since FP2 is immediately downstream of FP1, we now propose that FP1 and FP2 can be considered as two domains of an extended, bipartite FP (FP1_2). Comparatively, such an extended FP, consisting of 41 residues, is about twice the size of the influenza or HIV FPs (~20 residues). Both FP1 and FP2 possess membrane-ordering activity, and the extended FP (FP1_2) has only slightly higher membrane-ordering activity than that of individual FPs added together (FP1 + FP2). These observations suggest that while they function cooperatively, the FP1 and FP2 are structurally quite independent. Therefore, it may be appropriate to regard them as two subdomains of a bipartite "fusion platform."

Our data indicate that SARS-CoV S protein-induced membrane fusion is dependent on calcium. Our functional analyses using pseudotyped particles harboring full-length SARS-CoV S proteins show that the depletion of either extracellular or intracellular calcium significantly decreases SARS-CoV pseudovirion infectivity, indicating that S protein function is calcium dependent. Biophysical measurements performed in this work showed that the membrane-ordering activities of both FP1 and FP2 are only slightly affected by pH but are heavily dependent on calcium cations. We showed that the addition of EGTA eliminated the observed membrane-ordering effect. Furthermore, higher calcium concentrations were shown to enhance the membrane-ordering effect induced by both FP1 and FP2. The cooperativity of FP1 and FP2 is also calcium dependent. The ITC experiments on calcium–FP interactions not only demonstrated the interaction energy between calcium and both FP1 and FP2, but also showed that the stoichiometries are around 1 calcium cation per FP1 or FP2. Although the thermodynamics of the calcium interactions with FPs needs to be further investigated, our current data indicate a calcium dependency for S protein-induced membrane fusion, a dependency that stems from calcium–FP interactions.

Calcium ions are important modulators of membrane fusion. Because of their positive charges, they possess a generally enhancing or indirect effect on membrane fusion by electrostatic interactions with negatively charged headgroups of lipid bilayers, and thus decrease the electrostatic repulsion of two opposing membranes that are in close proximity prior to undergoing fusion. Calcium ions can also directly interact with fusion protein machineries, thereby activating their fusogenicity, and in such cases, membrane fusion is clearly calcium dependent. For example, in cellular SNARE-mediated synaptic vesicle fusion, calcium ions have been shown to be required activators for such fusion machinery [48–50]; that is, without calcium ions present, membrane fusion does not take place. Thus, SNARE-mediated synaptic membrane fusion is considered to be calcium dependent whereby calcium ions are fusion activators. There are other situations in which calcium cations have been shown to interact with protein fusogens and enhance their fusogenicity, but without calcium, membrane fusion can still occur albeit at a reduced rate. In such cases, membrane fusion is only partly dependent on calcium ions.

In the context of virus fusion, although it has been reported that the presence of calcium ions enhances viral FP-mediated vesicle-vesicle fusion, in most cases, the role of calcium is unlikely that of a fusion activator. In this study, we show that although calcium ions increase membrane-ordering effects in the influenza FP–membrane system, the increase mostly results from indirect effects of calcium ions by interacting with lipid headgroups and not through a direct interaction with the influenza FP, as demonstrated by the lack of variation of ΔS_0 values when calcium concentration increases (Fig. 5a). In such a case, calcium plays an indirect enhancing effect on membrane fusion. With HIV, calcium cations also enhance fusion, but such ions are not required, as HIV FP-mediated membrane fusion can still occur at a lower rate in the absence of calcium cations [51]. In contrast, for the Rubella virus, which belongs to the *Togaviridae* family of viruses and possesses a class II viral fusion protein containing two fusion loops, it has been shown that the E1 envelope glycoprotein specifically coordinates and requires a Ca^{2+} ion for low-pH-induced membrane insertion into liposomes [52].

Our analyses on SARS-CoV indicate a direct activating role for calcium for FP-mediated membrane fusion. We have shown that the membrane-ordering effect of the FPs is greatly reduced in presence of the EGTA chelator. Furthermore, increasing calcium concentrations enhance the membrane-ordering capacity of SARS-CoV FPs (i.e., ΔS_0 increases). We also show that the cooperative effect between FP1 and FP2 only occurs in the presence of calcium ions. Importantly, the interaction between calcium cations and FPs has been demonstrated by ITC. Finally, the intracellular calcium ion chelator BAPTA-AM was shown to abrogate viral entry in the *in vivo* assays we performed. Therefore, this study reveals that the activity of SARS-CoV S class I fusion protein is calcium dependent. Further efforts in our groups are ongoing to elucidate at the molecular level the mechanism by which the direct interaction between calcium ions and the SARS-CoV FP activates and enhances membrane fusion.

A proposed model for the SARS-CoV FP based on our observations and measurements is shown in Fig. 8. In this model, the bipartite FP or "platform" consists of two distinct subdomains FP1 and FP2, each binding to a calcium ion via negatively charged

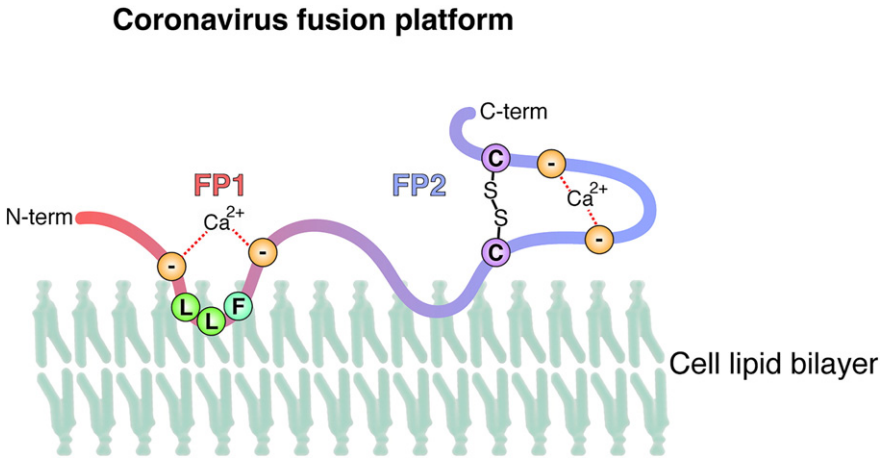

Fig. 8. Model of the CoV FP or "platform" interacting with a lipid bilayer. This model summarizes the data obtained in this work and highlights the unique features of this FP, including its bipartite nature and calcium-binding ability.

coordinating residues such as aspartic acids (D) and glutamic acids (E), found in clusters within each subdomain. The mechanism by which calcium specifically promotes FP-mediated membrane fusion is unclear. It is possible that within each subdomain, calcium ion coordination may allow the CoV FP to adopt a more compact conformation (Fig. 8). Such calcium coordination could also help the FP dock appropriately on the membrane surface. Further research on the details of the effects of calcium coordination with the CoV FP and on the cooperativity between FP1 and FP2 subdomains is required to shed light on this unusual viral FP.

Materials and Methods

Lipids and peptides

The lipids POPC, POPS, and the chain spin labels 5PC, 10PC, and 14PC and a head group spin label DPPTC were purchased from Avanti Polar Lipids (Alabaster, AL) or synthesized by our laboratory according to previous protocols. Chol was purchased from Sigma (St. Louis, MO). All peptides were synthesized by SynBioSci Co. (Livermore, CA). The shuffled sequences of rFP1 and rFP2 were generated using software Sequence Manipulation Suite (http://www.bioinformatics.org/sms2/shuffle_protein.html). The sequences of the peptides and the structure of the spin-labeled lipids are shown in Fig. 1.

Vesicle preparation

The composition of membranes used in this study is consistent with our previous study [14]. The desired amounts of POPC, POPS, Chol, and 0.5% (mol:mol) spin-labeled lipids in chloroform were mixed well and dried by N_2 flow. The mixture was evacuated in a vacuum drier overnight to remove any trace of chloroform. To prepare MLVs, the lipids were resuspended and fully hydrated using 1 mL of pH 7 or pH 5 buffer (5 mM HEPES, 10 mM MES, 150 mM NaCl, and 0.1 mM EDTA (pH 7 or pH 5)] at room temperature for 2 h. To reconstitute FP1 without GGGKKKK in membrane, the desired amounts of peptide were dissolved in 1,1,1,3,3,3-hexafluoro-2-propanol (Sigma) and well mixed with the lipids in chloroform. The mixtures were dried and fully hydrated to generate the MLVs. To prepare SUVs for CD and ITC measurements, the lipids were resuspended in pH 7 or pH 5 buffer and sonicated in an ice bath for 20 min or when the suspension became clear. The SUV solution was then further clarified by ultracentrifugation at 13,000 rpm for 10 min.

CD spectroscopy

The CD experiments were carried out on an AVIV CD spectrometer Aviv Model 215. The peptides were mixed with SUVs in 1% P/L ratio with a final peptide concentration of 0.1 mg/mL at room temperature for more than 10 min before the measurements. The measurements were performed at 25 °C and the averages of two repetitions were collected. Blanks were subtracted and the resulting spectra were analyzed. The mean residue weight ellipticity was calculated using the formula: $[\Theta] = \theta/(10 \times c \times l \times n)$, where θ is the ellipticity observed (in degrees), c is the peptide concentration (in dmol), l is the path length (0.1 cm), and n is the number of amino acids per peptide [27].

ITC

ITC experiments to measure the enthalpy of FPs membrane binding were performed in an N-ITC III calorimeter (TA Instrument, New Castle, DE). FP at 20 μM was injected into 1 mL 5 mM SUV solution at 37 °C. Each addition was 10 μL, each injection time was 15 s, and each interval time was 5 min. Each experiment comprised about 25 to 30 injections. The data were analyzed with Origin (OriginLab Corp., Northampton, MA).

ITC experiments to measure the peptide–Ca^{2+} interaction were performed in a VP-ITC MicroCalorimeter (MicroCal, LLC, Northampton, MA). $CaCl_2$ (2 mM) in pH 5 buffer was injected into 0.3 mM FPs in pH 5 buffer at 37 °C in a stepwise manner consisting of 10 μL per injection, except that the first injection was 2 μL. The injection time was 15 s for each injection and the interval time was 10 min. The data were analyzed with Origin. The one-site model was used in the fitting to calculate the thermodynamic parameters. The protein concentration is determined by dry weight and OD280 with extinction coefficient ε = 1490 M^{-1} cm^{-1} for FP1 and 1615 M^{-1} cm^{-1} for FP2 in the oxidized condition.

ESR spectroscopy and nonlinear least-squares fit of ESR spectra

To prepare the samples for lipid ESR study, the desired amounts of FPs (1 mg/mL) were added into the lipid MLV dispersion. After 20 min of incubation, the dispersion was spun at 13,000 rpm for 10 min. The concentrations of peptide were measured using UV to ensure complete binding of peptide. The pellet was transferred to a quartz capillary tube for ESR measurement. ESR spectra were collected on an ELEXSYS ESR spectrometer (Bruker Instruments, Billerica, MA) at X-band (9.5 GHz) at 25 °C using a N_2 Temperature Controller (Bruker Instruments).

The ESR spectra from the labeled lipids were analyzed using the NLLS fitting program based on the stochastic Liouville equation [39,53] using the MOMD model as in previous studies [21–25]. The fitting strategy is described below. We employed the Budil *et al*. NLLS fitting program [39] to obtain convergence to optimum parameters. The g-tensor and A-tensor parameters used in the simulations were determined from rigid limit spectra [21]. In the simulation, we required a good fit with a small value of χ^2 and also good agreement between the details of the final simulation and the experimental spectrum. Each experiment (and subsequent fit) was repeated 2 or 3 times to check reproducibility and estimate experimental uncertainty. Two sets of parameters that characterize the rotational diffusion of the nitroxide radical moiety in spin labels were generated. The first set is the rotational diffusion constants. $R_\perp$ and $R_\parallel$ are, respectively, the rates of rotation of the nitroxide moiety around a molecular axis perpendicular and parallel to the preferential orienting axis of the acyl chain. The second set consists of the ordering tensor parameters, S_0 and S_2, which are defined as follows: $S_0 = <D_{2,00}> = <1/2(3\cos 2\theta - 1)>$, and $S_2 = <D_{2,02} + D_{2,0-2}> = <\sqrt{(3/2)}\sin 2\theta \cos 2\varphi>$, where $D_{2,00}$, $D_{2,02}$, and $D_{2,0-2}$ are the Wigner rotation matrix elements and θ and φ are the polar and azimuthal angles for the orientation of the rotating axes of the nitroxide bonded to the lipid relative to the director of the bilayer, that is, the preferential orientation of lipid molecules; the angular brackets imply ensemble averaging. S_0 and its uncertainty were then calculated in a well-known fashion from its definition and the dimensionless ordering potentials C_{20} and C_{22} and their uncertainties found in the fitting. The typical uncertainties we find for S_0 range from 1 to 5×10^{-3}, while the uncertainties from repeated experiments are 5–8×10^{-3} or less than ±0.01. S_0 indicates how strongly the chain segment to which the nitroxide is attached is aligned along the normal to the lipid bilayer, which is strongly correlated with hydration/dehydration of the lipid bilayers. As previously described, S_0 is the more important parameter for such studies [23,54,55].

Bioinformatics sequence analyses

For generating protein sequence alignments, the following representative 42 CoV spike proteins and associated NCBI accession numbers were used: Alpaca-BCoV (ABI93999), AnteCoV-US/OH1/2003 (ABP38306), BatCoV-133/2005 (ABG47052), BatCoV-273/2005 (ABG47060), BatCoV-HKU4–1/2007 (ABN10839), BatCoV-HKU5–1/2007 (ABN10875), BatCoV-HKU10 (AFU92104), BatCoV-Neo/2011 (AGY29650), BatCoV-PDF-2180 (ARJ34226), BatCoV-SC2013/2013 (AHY61337), BCoV-Quebec (BAA00557), BdCoV-HKU22 (AHB63481), BeCoV-SW1 (ABW87820), BuCoV-HKU11 (ACJ12044), CamelAlphaCoV (ALA50256), CCoV-1-71 (AAV65515), CCoV-Elmo/02 (AAP72149), EquineCoV-NC99 (AAQ67205), EriCoV-VMC/DEU/2012 (AGX27810), FCoV-1683 (AFH58021), FCoV-RM (ACT10854), GiraCoV-US/OH3TC/2006 (ABP38313), HCoV-229E (AAK32188), HCoV-HKU1 (AAT98580), HCoV-NL63 (AGT51331), HCoV-OC43 (AAX84791), IBV-Beaudette (AAA70235), IBV-Cal99 (AAS00080), IBV-M41 (AAW33786), MERS-CoV-EMC/2012 (AFS88936), MERS-CoV-HKU205 (AHL18090), MHV-A59 (ACO72884), MHV-JHM (CAA28484), MuCoV-HKU13 (ACJ12062), PEDV-CV777 (AF353511_3), PHEV (AAL80031), PRCV-ISU-1 (ABG89317), SARS-CoV (AAP13441), TCoV-MG10 (ABW81427), TGEV-Miller-M6 (ABG89301), TGEV-Purdue (CAB91145), and ThCoV-HKU12 (ACJ12053). The protein sequences were aligned

using MUSCLE within the Geneious software suite and the aligned region corresponding to the SARS-CoV FP1 and FP2 was extracted. To highlight conserved and variable stretches within this region, a Weblogo was generated using Weblogo 3.0 software[†]. Invariant and highly conserved residues were highlighted.

Cells and reagents

HEK-293 T (ATCC, Manassas, VA) and Vero-E6 cells (ATCC) were grown at 37 °C 5% CO_2 in Dulbecco's modified Eagle medium (DMEM) containing Ca^{2+} cations (Corning, Corning, NY) supplemented with 10% fetal bovine serum (FBS; ThermoFisher, Waltham, MA), 10 mM Hepes (Corning), 100 IU/mL penicillin, and 100 μg/mL streptomycin (Corning). PBS with or without Ca^{2+} was obtained from Corning. DMEM without Ca^{2+} was used for functional analyses (ThermoFisher Scientific). EDTA chelating reagent was obtained from Corning. The cell membrane-permeable, calcium-specific chelator BAPTA-AM (acetoxymethyl ester) was obtained from ThermoFisher Scientific and used in functional assays. Stocks of BAPTA-AM were diluted in dimethyl sulfoxide (DMSO).

Pseudotyped virus production

Murine leukemia virus-based MERS-CoV S-pseudotyped particles, harboring wild-type SARS-CoV S protein, were generated as previously described [47]. Briefly, HEK-293 T cells were transfected with SARS-CoV S-encoding plasmid along with pCMV-MLVgag-pol packaging construct and the murine leukemia virus transfer vector encoding a luciferase reporter, using Lipofectamine 2000 transfection reagent (Life Technologies, Carlsbad, CA). The cells were incubated at 37 °C 5% CO_2 for 48 h (h), and supernatants were harvested, filtered through 0.45-μm membranes, and stored at −80 °C until used for infectivity assays.

Cell viability assays

Vero-E6 cells (2.5×10^4) were seeded in 96-well plates and incubated for 16 h at 37 °C 5% CO_2 incubator. The cells were treated with increasing concentrations of BAPTA-AM, from 0 μM (DMSO control) up to 50 μM. The treated cells were incubated at 37 °C 5% CO_2 for 2 h. After treatment growth medium was added to wells, cells were incubated for 72 h at 37 °C 5% CO_2 incubator. The cells were then lysed and viability assayed using the ATP-based CellTiter-Glo kit (Promega, Madison, WI) according to manufacturer's guidelines. Luminescence (relative luminescence units, or RLU) readings were performed using a GloMax 20/20 luminometer (Promega). The assays were carried out using triplicate wells, and data correspond to the average of three independent experiments. The percent cell viability was calculated by the following equation:

$$\%\text{cell viability} = 100 \times \frac{\text{RLU of BAPTA condition}}{\text{RLU of DMSO condition}}$$

Functional pseudotyped virus infectivity assays

Vero-E6 cells (1.5×10^5) were seeded in 24-well plates and incubated at 37 °C 5% CO_2 for 24 h. For extracellular calcium depletion assays, cells were washed twice with PBS with or without Ca^{2+}, and incubated with 200 μL of 2% FBS DMEM with or without Ca^{2+} for 2 h at 37 °C 5% CO_2. Supernatants were removed and 200 μL of SARSpp solution with or without EDTA (1.5 mM) was added to the cells for 2 h at 37 °C 5% CO_2. For experiments using BAPTA-AM intracellular calcium chelating reagent, cells were washed twice with PBS with or without Ca^{2+}, and incubated with a 200-μL solution of 2% FBS DMEM with either BAPTA-AM (50 μM) or DMSO for 2 h at 37 °C 5% CO_2. Supernatants were removed and 200 μL of SARSpp solution containing either BAPTA-AM (50 μM) or DMSO was added to the cells for 2 h at 37 °C 5% CO_2. For both types of assays, complete medium was then added and the cells were incubated at 37 °C for an additional 72 h. Luciferase activity was measured using Luciferase Assay Kit (Promega), and luminometer readings were performed with a GloMax 20/20 system (Promega).

Acknowledgments

This work was supported by grants from the National Institutes of Health, NIGMS, P41GM103521 and NIBIB R01EB003150 (to Jack H. Freed). This study was also supported by the National Institutes of Health Grant R21 AI111085 (to Gary R. Whittaker) and the Schwartz Research Fund for Women in the Life Sciences (to Susan Daniel). We thank Dr. Robert Oswald for enabling the use of the N-ITC III calorimeter and Dr. Brian Crane for the use of the AVIV CD spectrometer.

Received 21 June 2017;
Received in revised form 2 October 2017;
Accepted 12 October 2017
Available online 19 October 2017

Keywords:
membrane fusion;
viral entry;
electron spin resonance;
coronavirus;

†http://weblogo.berkeley.edu.

Abbreviations used:
BAPTA-AM, 1,2-bis(2-aminophenoxy)ethane-*N*,*N*,*N*′,*N*′-tetraacetic acid tetrakis; CD, circular dichroism; Chol, cholesterol; CoV, coronavirus; ESR, electron spin resonance; FP, fusion peptide; ITC, isothermal titration calorimetry; MERS, Middle East respiratory syndrome; MLVs, multilamellar vesicles; POPC, 1-palmitoyl-2-oleoyl-sn-glycero-3-phosphocholine; POPS, 1-palmitoyl-2-oleoyl-sn-glycero-3-phosphoserine; SARS, severe acute respiratory syndrome; SUVs, small unilamellar vesicles.

References

[1] J. White, J. Kartenbeck, A. Helenius, Membrane fusion activity of influenza virus, EMBO J. 1 (1982) 217–222 (http://www.ncbi.nlm.nih.gov/entrez/query.fcgi?cmd=Retrieve&db=PubMed&dopt=Citation&list_uids=7188182).

[2] S.B. Sieczkarski, G.R. Whittaker, Dissecting virus entry via endocytosis, J. Gen. Virol. 83 (2002) 1535–1545.

[3] J. Guillén, A.J. Pérez-Berná, M.R. Moreno, J. Villalaín, Identification of the membrane-active regions of the severe acute respiratory syndrome coronavirus spike membrane glycoprotein using a 16/18-mer peptide scan: implications for the viral fusion mechanism, J. Virol. 79 (2005) 1743–1752, https://doi.org/10.1128/JVI.79.3.1743-1752.2005.

[4] J. Guillén, P.K.J. Kinnunen, J. Villalaín, Membrane insertion of the three main membranotropic sequences from SARS-CoV S2 glycoprotein, Biochim. Biophys. Acta Biomembr. 1778 (2008) 2765–2774, https://doi.org/10.1016/j.bbamem.2008.07.021.

[5] I.G. Madu, S. Belouzard, G.R. Whittaker, SARS-coronavirus spike S2 domain flanked by cysteine residues C822 and C833 is important for activation of membrane fusion, Virology 393 (2009) 265–271, https://doi.org/10.1016/j.virol.2009.07.038.

[6] S. Belouzard, J.K. Millet, B.N. Licitra, G.R. Whittaker, Mechanisms of coronavirus cell entry mediated by the viral spike protein, Viruses 4 (2012) 1011–1033, https://doi.org/10.3390/v4061011.

[7] B. Sainz, J.M. Rausch, W.R. Gallaher, R.F. Garry, W.C. Wimley, Identification and characterization of the putative fusion peptide of the severe acute respiratory syndrome-associated coronavirus spike protein, J. Virol. 79 (2005) 7195–7206, https://doi.org/10.1128/JVI.79.11.7195-7206.2005.

[8] J.L. Lorieau, J.M. Louis, A. Bax, The complete influenza hemagglutinin fusion domain adopts a tight helical hairpin arrangement at the lipid:water interface, Proc. Natl. Acad. Sci. U. S. A. 107 (2010) 11341–11346 (doi:1006142107 [pii]10.1073/pnas.1006142107).

[9] X. Han, L.K. Tamm, pH-dependent self-association of influenza hemagglutinin fusion peptides in lipid bilayers, J. Mol. Biol. 304 (2000) 953–965 (http://www.ncbi.nlm.nih.gov/entrez/query.fcgi?cmd=Retrieve&db=PubMed&dopt=Citation&list_uids=11124039).

[10] X. Han, J.H. Bushweller, D.S. Cafiso, L.K. Tamm, Membrane structure and fusion-triggering conformational change of the fusion domain from influenza hemagglutinin, Nat. Struct. Biol. 8 (2001) 715–720 (http://www.ncbi.nlm.nih.gov/entrez/query.fcgi?cmd=Retrieve&db=PubMed&dopt=Citation&list_uids=11473264).

[11] S. Belouzard, V.C. Chu, G.R. Whittaker, Activation of the SARS coronavirus spike protein via sequential proteolytic cleavage at two distinct sites, Proc. Natl. Acad. Sci. U. S. A. 106 (2009) 5871–5876, https://doi.org/10.1073/pnas.0809524106.

[12] L.G.M. Basso, E.F. Vicente, E. Crusca, E.M. Cilli, A.J. Costa-Filho, SARS-CoV fusion peptides induce membrane surface ordering and curvature, Sci Rep 6 (2016), 37131. https://doi.org/10.1038/srep37131.

[13] M. Mahajan, S. Bhattacharjya, NMR structures and localization of the potential fusion peptides and the pre-transmembrane region of SARS-CoV: implications in membrane fusion, Biochim. Biophys. Acta Biomembr. 1848 (2015) 721–730, https://doi.org/10.1016/j.bbamem.2014.11.025.

[14] I.G. Madu, S.L. Roth, S. Belouzard, G.R. Whittaker, Characterization of a highly conserved domain within the severe acute respiratory syndrome coronavirus spike protein S2 domain with characteristics of a viral fusion peptide, J. Virol. 83 (2009) 7411–7421, https://doi.org/10.1128/JVI.00079-09.

[15] A.C. Walls, M.A. Tortorici, B.J. Bosch, B. Frenz, P.J. Rottier, F. DiMaio, F.A. Rey, D. Veesler, Cryo-electron microscopy structure of a coronavirus spike glycoprotein trimer, Nature 531 (2016) 114–117, https://doi.org/10.1038/nature16988.

[16] R.N. Kirchdoerfer, C.A. Cottrell, N. Wang, J. Pallesen, H.M. Yassine, H.L. Turner, K.S. Corbett, B.S. Graham, J.S. McLellan, A.B. Ward, Pre-fusion structure of a human coronavirus spike protein, Nature 531 (2016) 118–121, https://doi.org/10.1038/nature17200.

[17] A.C. Walls, M.A. Tortorici, B. Frenz, J. Snijder, W. Li, F.A. Rey, F. DiMaio, B.-J. Bosch, D. Veesler, Glycan shield and epitope masking of a coronavirus spike protein observed by cryo-electron microscopy, Nat. Struct. Mol. Biol. 23 (2016) 899–905, https://doi.org/10.1038/nsmb.3293.

[18] T. Panaretakis, O. Kepp, U. Brockmeier, A. Tesniere, A.C. Bjorklund, D.C. Chapman, M. Durchschlag, N. Joza, G. Pierron, P. van Endert, J. Yuan, L. Zitvogel, F. Madeo, D.B. Williams, G. Kroemer, Mechanisms of pre-apoptotic calreticulin exposure in immunogenic cell death, EMBO J. 28 (2009) 578–590 (doi:emboj20091 [pii]10.1038/emboj.2009.1).

[19] M. Gui, W. Song, H. Zhou, J. Xu, S. Chen, Y. Xiang, X. Wang, Cryo-electron microscopy structures of the SARS-CoV spike glycoprotein reveal a prerequisite conformational state for receptor binding, Cell Res. 27 (2017) 119–129, https://doi.org/10.1038/cr.2016.152.

[20] Y. Yuan, D. Cao, Y. Zhang, J. Ma, J. Qi, Q. Wang, G. Lu, Y. Wu, J. Yan, Y. Shi, X. Zhang, G.F. Gao, Cryo-EM structures of MERS-CoV and SARS-CoV spike glycoproteins reveal the dynamic receptor binding domains, Nat. Commun. 8 (2017), 15092. https://doi.org/10.1038/ncomms15092.

[21] M. Ge, J.H. Freed, Fusion peptide from influenza hemagglutinin increases membrane surface order: an electron-spin resonance study, Biophys. J. 96 (2009) 4925–4934 (doi:S0006–3495(09)00802–9 [pii]10.1016/j.bpj.2009.04.015).

[22] M. Ge, J.H. Freed, Two conserved residues are important for inducing highly ordered membrane domains by the transmembrane domain of influenza hemagglutinin, Biophys. J. 100 (2011) 90–97 (doi:S0006–3495(10)01383–4 [pii]10.1016/j.bpj.2010.11.014).

[23] A.L. Lai, J.H. Freed, Interaction between the influenza HA fusion peptide and transmembrane domain affects membrane structure, Biophys. J. 109 (2015) 1–14.

[24] A.L. Lai, J.H. Freed, HIV gp41 fusion peptide increases membrane ordering in a cholesterol-dependent fashion, Biophys. J. 106 (2014) 172–181, https://doi.org/10.1016/j.bpj.2013.11.027S0006-3495(13)01262-9 (pii).

[25] J.F. Pinello, A.L. Lai, J.K. Millet, D. Cassidy-Hanley, J.H. Freed, T.G. Clark, Structure–function studies link class II viral fusogens with the ancestral gamete fusion protein HAP2, Curr. Biol. 27 (2017) 651–660, https://doi.org/10.1016/j.cub.2017.01.049.

[26] M. Ge, J.H. Freed, Hydration, structure, and molecular interactions in the headgroup region of dioleoylphosphatidylcholine bilayers: an electron spin resonance study, Biophys. J. 85 (2003) 4023–4040, https://doi.org/10.1016/S0006-3495(03)74816-4.

[27] A.L. Lai, H. Park, J.M. White, L.K. Tamm, Fusion peptide of influenza hemagglutinin requires a fixed angle boomerang structure for activity, J. Biol. Chem. 281 (2006) 5760–5770 (http://www.ncbi.nlm.nih.gov/entrez/query.fcgi?cmd=Retrieve&db=PubMed&dopt=Citation&list_uids=16407195).

[28] X. Han, D.A. Steinhauer, S.A. Wharton, L.K. Tamm, Interaction of mutant influenza virus hemagglutinin fusion peptides with lipid bilayers: probing the role of hydrophobic residue size in the central region of the fusion peptide, Biochemistry 38 (1999) 15052–15059 (http://www.ncbi.nlm.nih.gov/entrez/query.fcgi?cmd=Retrieve&db=PubMed&dopt=Citation&list_uids=10555988).

[29] G. van Meer, D.R. Voelker, G.W. Feigenson, Membrane lipids: where they are and how they behave, Nat. Rev. Mol. Cell Biol. 9 (2008) 112–124, https://doi.org/10.1038/nrm2330.

[30] A.L. Lai, L.K. Tamm, J.F. Ellena, D.S. Cafiso, Synaptotagmin 1 modulates lipid acyl chain order in lipid bilayers by demixing phosphatidylserine, J. Biol. Chem. 286 (2011) 25291–25300 (doi:M111.258848 [pii]10.1074/jbc.M111.258848).

[31] S. Takamori, M. Holt, K. Stenius, E.A. Lemke, M. Gronborg, D. Riedel, H. Urlaub, S. Schenck, B. Brugger, P. Ringler, S.A. Muller, B. Rammner, F. Grater, J.S. Hub, B.L. De Groot, G. Mieskes, Y. Moriyama, J. Klingauf, H. Grubmuller, J. Heuser, F. Wieland, R. Jahn, Molecular anatomy of a trafficking organelle, Cell 127 (2006) 831–846 (doi:S0092–8674(06)01400–0 [pii]10.1016/j.cell.2006.10.030).

[32] A.A. Frazier, C.R. Roller, J.J. Havelka, A. Hinderliter, D.S. Cafiso, Membrane-bound orientation and position of the synaptotagmin I C2A domain by site-directed spin labeling, Biochemistry 42 (2003) 96–105 (http://www.ncbi.nlm.nih.gov/entrez/query.fcgi?cmd=Retrieve&db=PubMed&dopt=Citation&list_uids=12515543).

[33] A. Patel, B.-P. Mohl, P. Roy, Entry of bluetongue virus capsid requires the late endosome-specific lipid lysobisphosphatidic acid, J. Biol. Chem. 291 (2016) 12408–12419, https://doi.org/10.1074/jbc.M115.700856.

[34] P.M. Matos, M. Marin, B. Ahn, W. Lam, N.C. Santos, G.B. Melikyan, Anionic lipids are required for vesicular stomatitis virus G protein-mediated single particle fusion with supported lipid bilayers, J. Biol. Chem. 288 (2013) 12416–12425, https://doi.org/10.1074/jbc.M113.462028.

[35] E. Zaitseva, E. Zaitsev, K. Melikov, A. Arakelyan, M. Marin, R. Villasmil, L.B. Margolis, G.B. Melikyan, L.V. Chernomordik, Fusion stage of HIV-1 entry depends on virus-induced cell surface exposure of Phosphatidylserine, Cell Host Microbe 22 (2017) 99–110.e7, https://doi.org/10.1016/j.chom.2017.06.012.

[36] Y. Hu, S. Patel, Thermodynamics of cell-penetrating HIV1 TAT peptide insertion into PC/PS/CHOL model bilayers through transmembrane pores: the roles of cholesterol and anionic lipids, Soft Matter 12 (2016) 6716–6727, https://doi.org/10.1039/c5sm01696g.

[37] R. Yang, M. Prorok, F.J. Castellino, D.P. Weliky, A trimeric HIV-1 fusion peptide construct which does not self-associate in aqueous solution and which has 15-fold higher membrane fusion rate, J. Am. Chem. Soc. 126 (2004) 14722–14723 (http://www.ncbi.nlm.nih.gov/entrez/query.fcgi?cmd=Retrieve&db=PubMed&dopt=Citation&list_uids=15535688).

[38] M. Ge, D.E. Budil, J.H. Freed, An electron spin resonance study of interactions between phosphatidylcholine and phosphatidylserine in oriented membranes, Biophys. J. 66 (1994) 1515–1521, https://doi.org/10.1016/S0006-3495(94)80942-7.

[39] D.E. Budil, S. Lee, S. Saxena, J.H. Freed, Nonlinear-least-squares analysis of slow-motion EPR spectra in one and two dimensions using a modified Levenberg-Marquardt algorithm, J. Magn. Reson. Ser. A 120 (1996) 155–189.

[40] Y. Lou, M. Ge, J. Freed, A multifrequency ESR study of the complex dynamics of membranes, J. Phys. Chem. B 105 (2001) 11053–11056.

[41] J. Seelig, S. Nebel, P. Ganz, C. Bruns, Electrostatic and nonpolar peptide–membrane interactions—lipid-binding and functional-properties of somatostatin analogs of charge Z = +1 to Z = +3, Biochemistry 32 (1993) 9714–9721.

[42] Y. Li, X. Han, L.K. Tamm, Thermodynamics of fusion peptide–membrane interactions, Biochemistry 42 (2003) 7245–7251 (http://www.ncbi.nlm.nih.gov/entrez/query.fcgi?cmd=Retrieve&db=PubMed&dopt=Citation&list_uids=12795621).

[43] J. Yang, C.M. Gabrys, D.P. Weliky, Solid-state nuclear magnetic resonance evidence for an extended beta strand conformation of the membrane-bound HIV-1 fusion peptide, Biochemistry 40 (2001) 8126–8137 (http://www.ncbi.nlm.nih.gov/entrez/query.fcgi?cmd=Retrieve&db=PubMed&dopt=Citation&list_uids=11434782).

[44] M. Ge, J.H. Freed, An electron spin resonance study of interactions between gramicidin a' and phosphatidylcholine bilayers, Biophys. J. 65 (1993) 2106–2123, https://doi.org/10.1016/S0006-3495(93)81255-4.

[45] A.L. Lai, L.K. Tamm, Locking the kink in the influenza hemagglutinin fusion domain structure, J. Biol. Chem. 282 (2007) 23946–23956 (doi:M704008200 [pii]10.1074/jbc.M704008200).

[46] S.C. Brennan, W.J. Wilkinson, H.-E. Tseng, B. Finney, B. Monk, H. Dibble, S. Quilliam, D. Warburton, L.J. Galietta, P.J. Kemp, D. Riccardi, The extracellular calcium-sensing receptor regulates human fetal lung development via CFTR, Sci Rep 6 (2016), 21975. https://doi.org/10.1038/srep21975.

[47] J.K. Millet, G.R. Whittaker, Murine leukemia virus (MLV)-based coronavirus spike-pseudotyped particle production and infection, Bio-Protocol. 6 (2016)https://doi.org/10.21769/BioProtoc.2035.

[48] A. Bhalla, M.C. Chicka, W.C. Tucker, E.R. Chapman, Ca(2+)-synaptotagmin directly regulates t-SNARE function during reconstituted membrane fusion, Nat. Struct. Mol. Biol. 13 (2006) 323–330 (doi:nsmb1076 [pii]10.1038/nsmb1076).

[49] A.T. Brunger, Structure and function of SNARE and SNARE-interacting proteins, Q. Rev. Biophys. 38 (2005) 1–47 (http://www.ncbi.nlm.nih.gov/entrez/query.fcgi?cmd=Retrieve&db=PubMed&dopt=Citation&list_uids=16336742).

[50] M.C. Chicka, E. Hui, H. Liu, E.R. Chapman, Synaptotagmin arrests the SNARE complex before triggering fast, efficient membrane fusion in response to Ca2+, Nat. Struct. Mol. Biol. 15 (2008) 827–835 (doi:nsmb.1463 [pii]10.1038/nsmb.1463).

[51] T. Suarez, W.R. Gallaher, A. Agirre, F.M. Goni, J.L. Nieva, Membrane interface-interacting sequences within the ectodomain of the human immunodeficiency virus type 1 envelope glycoprotein: putative role during viral fusion, J. Virol. 74 (2000) 8038–8047 (http://www.ncbi.nlm.nih.gov/entrez/query.fcgi?cmd=Retrieve&db=PubMed&dopt=Citation&list_uids=10933713).

[52] M. Dubé, F.A. Rey, M. Kielian, Rubella virus: first calcium-requiring viral fusion protein, PLoS Pathog. 10 (2014), e1004530. https://doi.org/10.1371/journal.ppat.1004530.

[53] M. Ge, D.E. Budil, J.H. Freed, ESR studies of spin-labeled membranes aligned by isopotential spin-dry ultracentrifugation: lipid–protein interactions, Biophys. J. 67 (1994) 2326–2344, https://doi.org/10.1016/S0006-3495(94)80719-2.

[54] M. Ge, K.A. Field, R. Aneja, D. Holowka, B. Baird, J.H. Freed, Electron spin resonance characterization of liquid ordered phase of detergent-resistant membranes from RBL-2H3 cells, Biophys. J. 77 (1999) 925–933, https://doi.org/10.1016/S0006-3495(99)76943-2.

[55] M. Ge, A. Gidwani, H.A. Brown, D. Holowka, B. Baird, J.H. Freed, Ordered and disordered phases coexist in plasma membrane vesicles of RBL-2H3 mast cells. An ESR study, Biophys. J. 85 (2003) 1278–1288 (doi:S0006–3495(03)74563–9 [pii]10.1016/S0006-3495(03)74563-9).